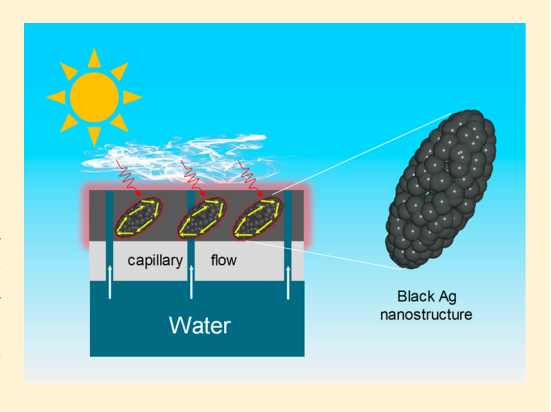
Downloaded via UNIV OF CALIFORNIA RIVERSIDE on July 31, 2019 at 06:41:47 (UTC). See https://pubs.acs.org/sharingguidelines for options on how to legitimately share published articles.

# Space-Confined Seeded Growth of Black Silver Nanostructures for **Solar Steam Generation**

Jinxing Chen,<sup>†,‡</sup> Ji Feng,<sup>‡</sup> Zhiwei Li,<sup>‡</sup> Panpan Xu,<sup>‡</sup> Xiaojing Wang,<sup>‡</sup> Wenwen Yin,<sup>‡</sup> Mozhen Wang,\*<sup>†</sup>
Xuewu Ge,<sup>†</sup> and Yadong Yin\*<sup>‡</sup>

Supporting Information

ABSTRACT: Plasmonic metal nanostructures have attracted considerable attention for solar energy harvesting due to their capability in photothermal conversion. However, the narrow resonant band of the conventional plasmonic nanoparticles greatly limits their application as only a small fraction of the solar energy can be utilized. Herein, a unique confined seeded growth strategy is developed to synthesize black silver nanostructures with broadband absorption in the visible and near-infrared spectrum. Through this novel strategy, assemblages of silver nanoparticles with widely distributed interparticle distances are generated in rod-shaped tubular spaces, leading to strong random plasmonic coupling and accordingly broadband absorption for significantly improved utilization of solar energy. With excellent efficiency in converting solar energy to heat, the resulting black Ag nanostructures can be made into thin films floating at the air/water interface for efficient generation of clean water steam through localized interfacial heating.



KEYWORDS: Space-confined synthesis, seeded growth, black silver, broadband absorption, photothermal, steam generation

n the past ten years, over one-third of the world's population lives in water-stressed countries. And by 2025, this figure is predicted to rise to nearly two-thirds. Among various technologies designed for augmenting available water resources, strategies based on the photothermal effect have gained increasing attention for clean water generation.<sup>2-5</sup> Under the photothermal scheme, solar light can be harvested by light-absorbing materials and then converted into heat, which further induces steam generation. For effective solar steam generation, it is critical to design the light-absorbing materials to make the best use of sunlight by maximizing the absorption and minimizing the reflectance and transmittance of the light.

Plasmonic metal nanostructures have been previously studied for harvesting solar energy.<sup>6-9</sup> When light interacts with plasmonic nanostructures, the portion with the resonant frequency can be either scattered, which causes the re-emission of light, or absorbed, which leads to heat generation. One of the advantageous features of plasmonic nanomaterials for solar steam generation is that their plasmonic property can be widely modulated by engineering their structural configuration, making it possible to enhance the absorption of incident photons and their conversion into heat and in the meantime to reduce their scattering through radiative decay. 10-12 For example, it has been pointed out that the efficiency of the photothermal conversion of gold nanoparticles can be

enhanced by reducing their sizes. 12 However, simply controlling the particle size is not sufficient for building an efficient solar steam generation system because the narrowband plasmonic resonance of metal nanoparticles only allows the utilization of a small portion of light in the solar spectrum. It is therefore highly desirable to design plasmonic materials with broadband light absorption to significantly enhance the conversion efficiency from sunlight to heat. 13-15

One of the most effective strategies to broaden the absorption bandwidth and boost electron oscillations is to induce plasmonic coupling. 16,17 When two plasmonic nanoparticles come sufficiently close, their resonance modes start to hybridize, causing a red shift and broadening of their resonance band. The magnitude of the coupling depends on the interparticle distance. However, plasmonic coupling in shortrange or in a simple interacting system can only cause small spectral broadening, 14,18 making it still inefficient in solar energy utilization. While many previous studies aim to achieve uniform interparticle spacing and narrow plasmonic band, for the application of solar steam generation, it is highly desirable to design effective fabrication strategies toward plasmonic

Received: October 16, 2018 Revised: December 13, 2018 Published: December 18, 2018

Department of Polymer Science and Engineering, University of Science and Technology of China, Hefei, Anhui 230026, P. R.

<sup>\*</sup>Department of Chemistry, University of California Riverside, Riverside, California 92521, United States

nanomaterials with widely distributed interparticle spacing so that random plasmonic coupling could be induced to absorb more solar light. 11

In this work, we report an effective seeded growth method to prepare plasmonic silver (Ag) nanostructures within confined spaces to achieve well distributed interparticle distance for random plasmonic coupling. Seeded growth has been conventionally used for the synthesis of colloidal dispersions of noble metal nanoparticles with controlled sizes and shapes. 19,20 In order to create random plasmonic coupling, we fix the seeds on a nanoscale substrate within a confined tubular space and keep them separated in a short distance. Subsequent growth of the seeds gradually decreases the interparticle separation and at the same time enhances the plasmonic coupling, leading to the formation of Ag nanoparticle (AgNP) assemblages with large absorption cross-section which can maximize the absorption of incident visible and near-IR lights. More importantly, since the seeds are loaded inside the tubular space without any specific order, the interparticle coupling could happen along either longitudinal or transverse directions, leading to random plasmonic coupling and subsequently broadband absorption. We further take advantage of this unique structural design and demonstrate the application of the AgNP assemblages in solar steam generation for water purification.

The seeded growth of Ag nanostructures within a confined tubular space could enhance the plasmonic coupling effect of AgNPs. The seeds were defined within tubular nanorods through a hard-templating method. First, uniform ellipsoidal iron oxyhydroxide (FeOOH) nanorods with average dimensions of  $125 \times 25$  nm (AR = 5) were prepared as the initial templates through direct hydrolysis of FeCl<sub>3</sub> in an aqueous solution. Subsequently, Au seeds (1-3 nm) were synthesized using a simple reduction process and then attached to the surface of the FeOOH nanorods. For enhancing the binding affinity of Au seeds to FeOOH nanorods, the nanorod surface was premodified with polyethylenimine (PEI), which binds strongly to both and can serve as an effective bridging layer. As shown in Figure 1a, the Au seeds were randomly attached to the surface of FeOOH nanorods. The high loading density of the Au seeds ensured the plasmonic coupling after the seeded growth procedure. To create the tubular space, we further coated the FeOOH/Au nanorods with a layer of resorcinolformaldehyde (RF). As shown in Figure 1b, a layer of RF with a thickness of 27 nm was deposited on the surface of composite nanorods uniformly. RF was chosen as the shell material because the cross-linked polymer not only maintained the original shape after removing the template but also exhibited relatively good molecular permeability. In order to create the hollow template, we removed FeOOH nanorods by etching with oxalic acid at 80 °C for 3 h. As shown in Figure 1c, rodlike RF nanotubes were obtained with Au seeds decorated on the inner walls.

When the reduction of  $Ag^+$  was initiated, a significant number of metal atoms formed rapidly. These newly formed Ag atoms either deposit on the existing seeds or nucleate by themselves to eventually form free AgNPs. In this case, the chance of self-nucleation is high as the RF shell hinders the diffusion of  $Ag^+$  ions to the inner part of the polymer shell. In order to prevent self-nucleation, we reduced the reduction potential of the Ag precursor by complexing it with acetonitrile  $(ACN)^{21,22}$  and further decreased the reaction rate by slowly pumping the complex solution into the reaction system using a syringe pump at a low injection rate (5  $\mu$ L/min). As shown in

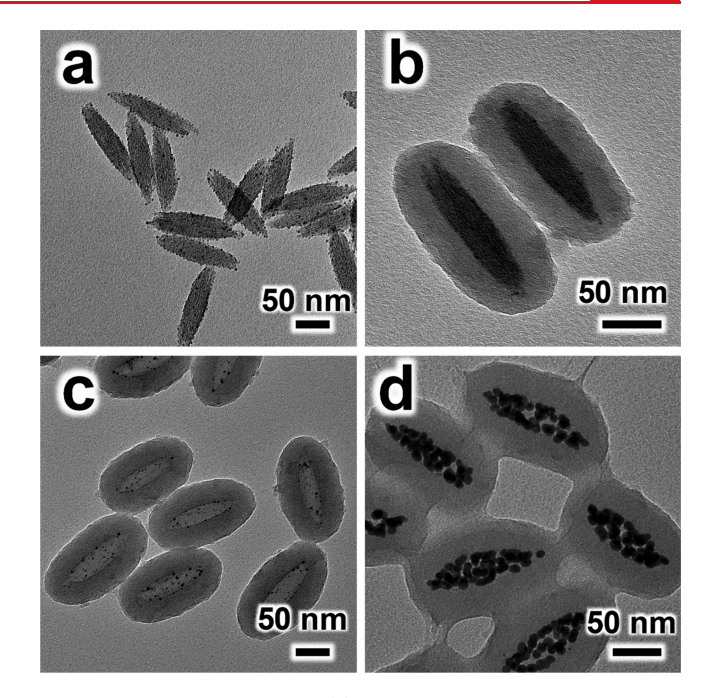


**Figure 1.** TEM images of (a) FeOOH nanorods with surface modified with Au seeds, (b) FeOOH/Au nanorods overcoated with a layer of RF, (c) hollow RF nanorods containing Au seeds on the inner surface prepared by removing FeOOH, and (d) RF nanorods with AgNP assemblages upon growth of Ag on Au seeds.

Figure 1d, after 7 min of continuous injection, an assemblage of AgNPs was formed in each tubular space, taking an overall rod shape. Careful inspection suggests that the small AgNPs (<10 nm) are separated from each other, with an interparticle gap less than 3 nm. The colloidal solution after the seeded growth appeared to be black, indicating the full-spectrum absorption of the nanostructures in the visible range.

Parts a-d of Figure 2 show the evolution of Ag nanostructures with increasing amounts of Ag precursors. In this case, the particle size and consequently the interparticle distance can be manipulated by controlling the extent of growth. With the addition of a small amount of Ag-ACN complex (15  $\mu$ L), the seeds did not grow substantially so that the interparticle separation remained much larger than the dimension of the resulting AgNPs, leading to insignificant interparticle plasmonic coupling. The light yellow color (inset in Figure 2a) and the unimodal extinction peak around 430 nm (Figure 2f) confirmed the contribution of plasmonic resonance of isolated AgNPs and the lack of plasmonic coupling among them. When 25  $\mu$ L of Ag-ACN complex was introduced into the reaction system, we obtained a dark green solution showing the development of a new peak at a longer wavelength (~600 nm) in the UV-vis-NIR extinction spectra, which indicates the occurrence of plasmonic coupling. On the basis of Figure 2b, we estimated the interparticle distance of 3-7 nm, which is expected to induce strong coupling according to Mie's theory. With an increased amount of Ag-ACN precursor of 35  $\mu$ L, the solution changed to entirely black. At a decreased interparticle gap of less than 2 nm (Figure 2c), strong coupling was caused between adjacent AgNPs due to the boosted absorption crosssection area. When the Ag-ACN precursor was further increased to 65  $\mu$ L, the extensive growth of AgNPs led to their fusion with each other (Figure 2d), producing effectively Ag nanorods with two pronounced resonance peaks, one at

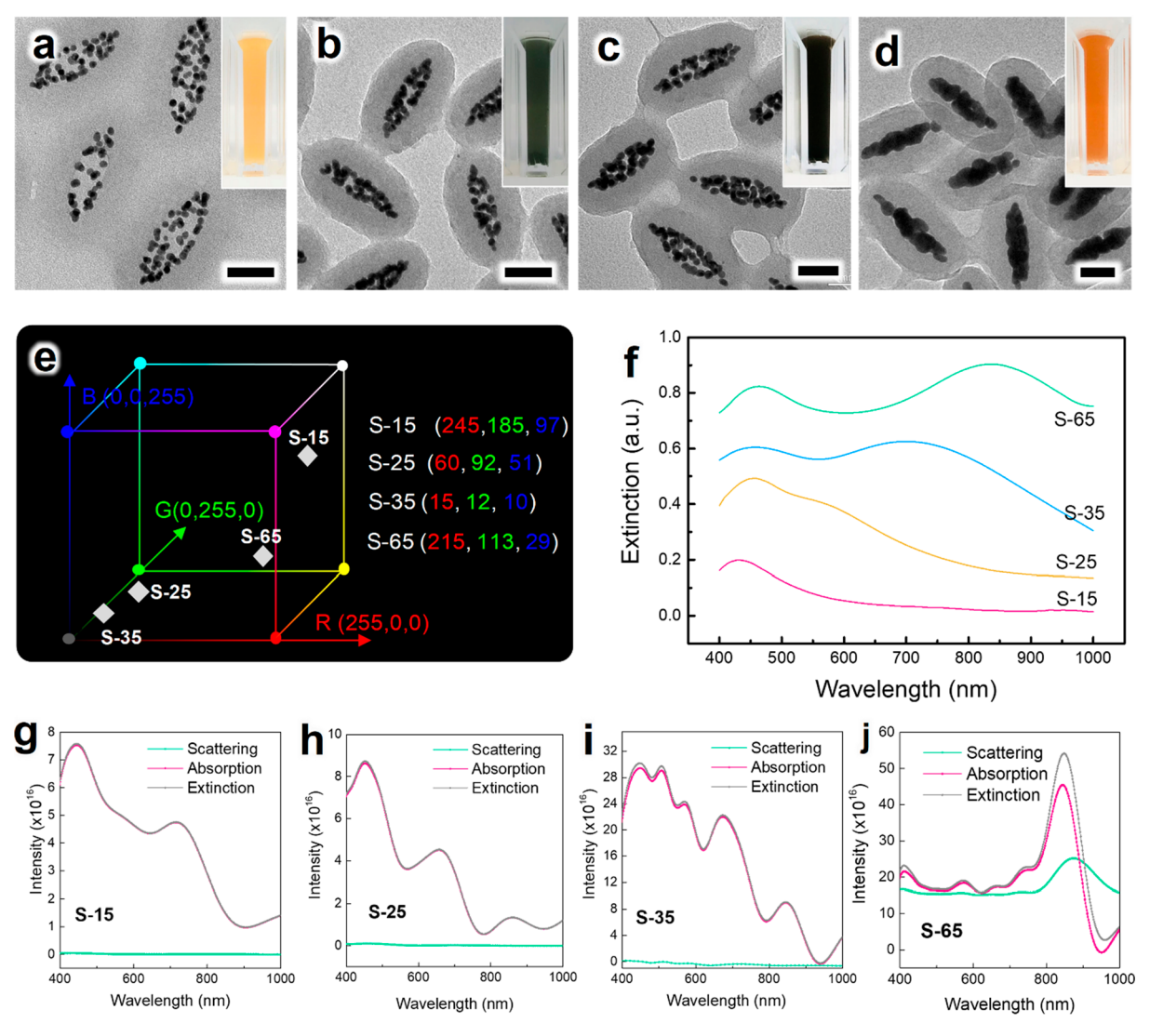


Figure 2. (a)—(d) TEM images of the samples prepared by injection of 15  $\mu$ L (a, named as S-15), 25  $\mu$ L (b, S-25), 35  $\mu$ L (c, S-35), and 65  $\mu$ L (d, S-65) of precursor solution with an injection rate of 5  $\mu$ L/min. Scale bars are all 50 nm. Insets are the digital photos of the corresponding colloidal dispersions. (e) Position of each color in the RGB cube, obtained by extracting the relative component of red, green, and blue from the corresponding digital photos using ImageJ software. (f) UV—vis—NIR extinction spectra of the colloidal dispersions. (g)—(j) Spectra simulated using the finite-difference time-domain (FDTD) method based on the TEM images of the products.

~470 nm corresponding to the transverse mode and the other at 850 nm to the longitudinal mode. As the latter lies in the near-IR, the solution appeared to be orange in color, as determined primarily by the transverse resonance mode.

The displayed color of the samples can be set in an RGB cube for better understanding the absorption behaviors. In the RGB cube, the diagonal connects the darkest point (0, 0, 0) in the cube with the brightest one (255, 255, 255). As shown in Figure 2e, S-15 and S-65 are close to the brightest point. While S-25 is weak in red and blue, its green is relatively strong. Among all the samples, only S-35 displays the color on the diagonal and near the darkest point, indicating that it has an equal ability to absorb red, green, and blue light. In other words, S-35 is strong in broadband absorption.

It is well-known that the total extinction profile, as determined by UV-vis-NIR spectrometry, is contributed by both absorption and scattering, while only the absorbed light can be converted to heat. Therefore, we performed simulation by FDTD solution to evaluate the contribution of absorption to extinction for each sample. As shown in Figure 2g-j, the

absorption cross-section of the AgNP assemblages dominates the extinction cross section area when the addition of Ag-ACN is less than 35  $\mu$ L. When the AgNPs grow to the point where interconnections occur, the resulting larger domains (~30 nm) scatter more incident light and lead to lower usage of the solar energy (Figure 2j). While in principle the plasmonic nanostructures with small sizes (less 20 nm) show dominant absorption characteristics, their isolated form only has a small overlap with the sunlight spectrum. In our strategy, integrating small AgNPs within a confined space not only guarantees the larger ratio of absorption and extinction (around 100%) but also achieves broadband absorption through the random coupling, both are beneficial to the utilization of the solar energy. More importantly, our confined seeded growth strategy allows convenient control of the plasmonic coupling by manipulating the particle size and interparticle distance, making it possible to further optimize the energy harvesting

Another essential feature that our synthesis strategy can offer is the overall anisotropic shape of the assemblages, which is

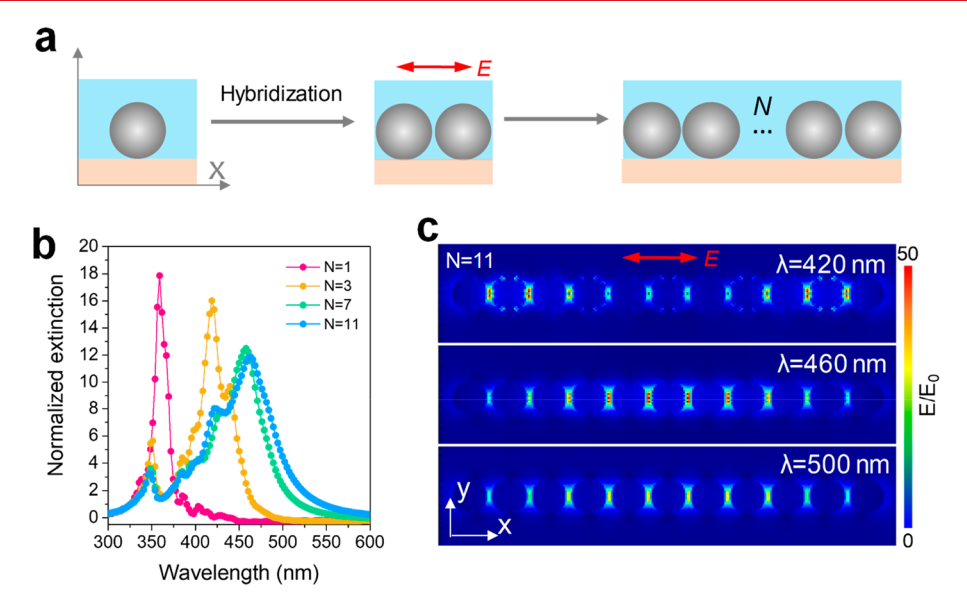


Figure 3. (a) Schematic illustration of the model considered in FDTD simulation. (b) Simulated extinction profile of AgNP chains of varying lengths. The intensity is normalized against the number of nanoparticles. (c) Near electromagnetic field of AgNP chains (N = 11) excited by incident light of varying wavelengths (420, 460, and 500 nm).

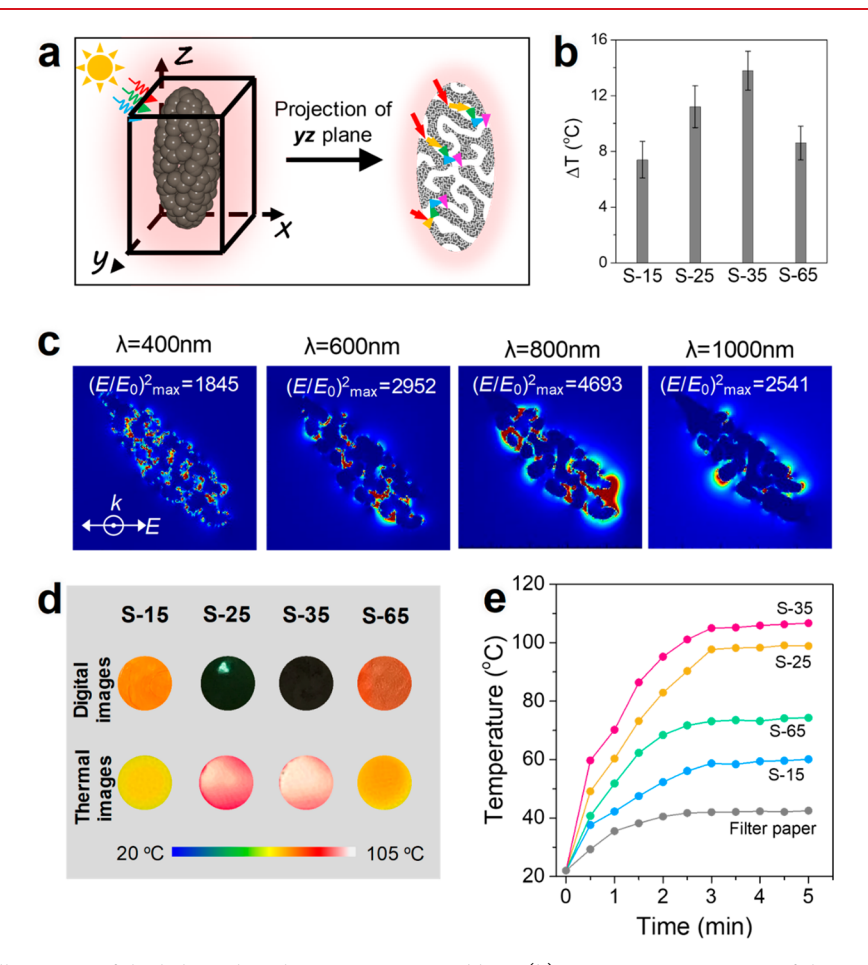


Figure 4. (a) Schematic illustration of the light path within an AgNP assemblage. (b) Temperature variation of the nanostructure dispersion (25  $\mu$ g/mL) under the illumination of xenon light (300 W) for 1 min. (c) Distribution of near electromagnetic field of S-35 at different wavelengths. (d) Digital and thermal images of filter paper deposited with various Ag nanostructures. The thermal images of films were recorded by a thermal camera after irradiated with xenon light (300 W) for 5 min. (e) Temperature change over time when different films were subjected to the illumination of xenon light (300 W).

defined by the tubular RF templates. Compared with isotropic ones, the anisotropic assemblages help to produce more

complex and random plasmonic coupling, since the electron resonance may occur in both longitudinal and transverse

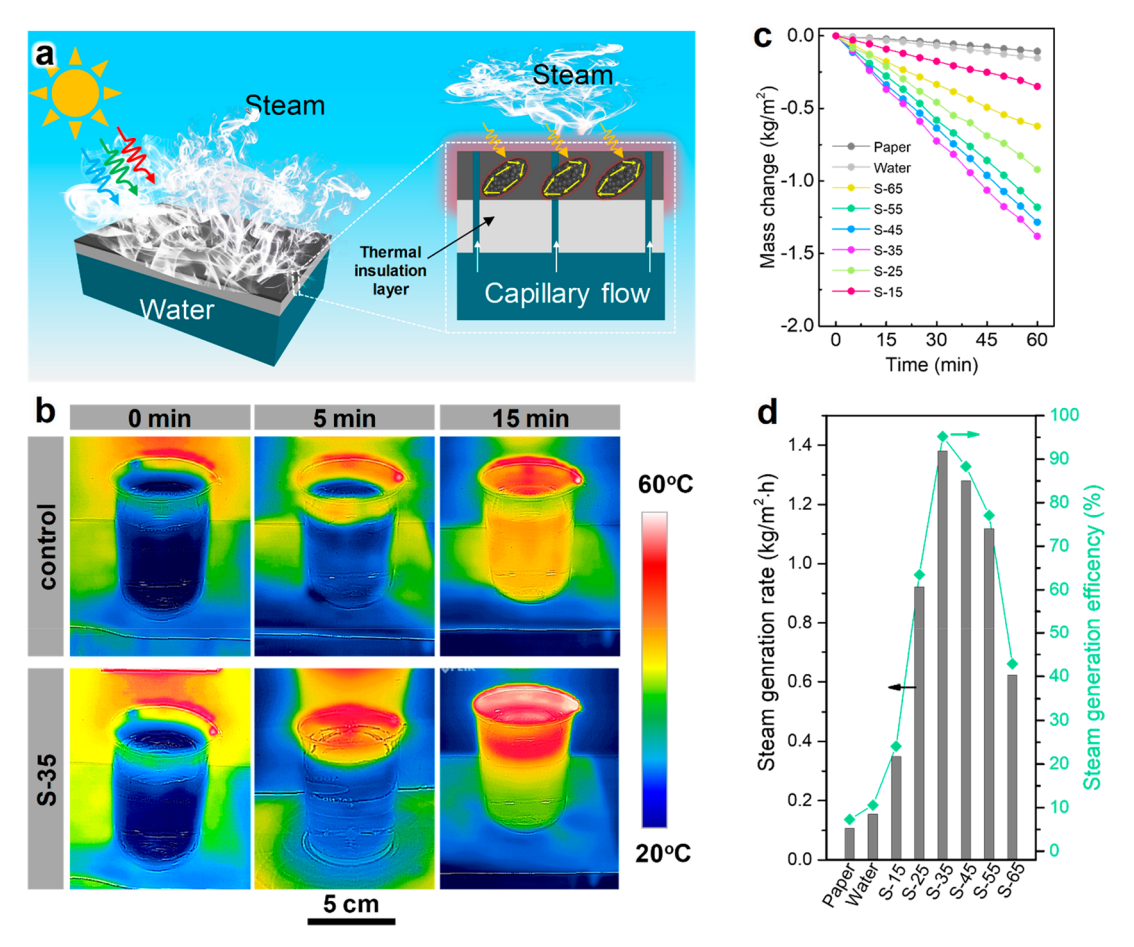


Figure 5. (a) Schematic illustration of the solar steam generation process. (b) IR thermal images of water beakers recorded by a thermal camera after being irradiated with a xenon light (300 W) for different periods of time without (top panel) and with (bottom panel) a black film of AgNP assemblages. (c) Time course of water evaporation performance under various conditions. (d) Dependence of the steam generation rate and efficiency on the amount of AgNO<sub>3</sub> precursor used in the seeded growth.

directions. To further illustrate this effect, we again performed simulation by using FDTD solution, where a one-dimensional (1D) array of AgNPs was used as a simplified model to represent the complex anisotropic assemblages. As schematically shown in Figure 3a, the 1D array of AgNPs are arranged along the x-axis with the incident light from the z-axis. The diameter of AgNPs and interparticle distance are set at 20 and 2 nm, respectively. Figure 3b shows the length-dependent plasmonic absorption profile of AgNP array in vacuum. While a single AgNP exhibits a unimodal and sharp peak at 360 nm, the extinction peak broadens and red-shifts to 420 nm once three AgNPs are involved in the array, indicating the hybridization of resonance of individual particles. The peak broadening and red shift continue when more AgNPs are involved in the array (N = 7 and N = 11). The interparticle plasmonic coupling can also be visualized in FDTD solution by using a two-dimensional frequency-domain field profile. As shown in Figure 3c, when the incident lights with wavelengths of 420, 460, and 500 nm irradiate an 11-unit array along the xaxis, the near electromagnetic field shows great enhancement at the gap areas, demonstrating effective plasmonic coupling along the array direction. In contrast, the weak plasmonic coupling could be found in the system when the incident lights irradiate an 11-unit array along the y-axis (Figure S1), which also confirms the anisotropic plasmonic coupling. Although the 1D array is only an extremely simplified model of the actual

rodlike assemblage, the simulation results still suggest the important contribution of the anisotropic morphology to the random plasmonic coupling.

The as-prepared Ag nanostructures show strong random coupling that is beneficial to sunlight harvesting. In addition, as schematically shown in Figure 4a, the porosity in AgNP assemblages may also play a helpful role in energy conversion through the possible multireflection processes during the complicated light—matter interaction. <sup>23,24</sup> In every light—matter interaction, a part of the incident solar energy is converted to heat through the photothermal effect. Figure 4b shows the temperature change of water containing the four types of samples (25  $\mu$ g/mL) under the illumination of the xenon light for 1 min. As expected, S-35 exhibited the most significant temperature elevation of 14 °C, which agreed well with the results shown in Figure 2.

A key feature of the as-synthesized AgNP assemblages is their random coupling, which ensures broadband absorption in the visible and near-IR spectrum (Figure S2). To support our understanding, we have used FDTD solution to study the distribution of the near electromagnetic field when lights of various wavelengths interact with S-35. As demonstrated in Figure 4c, the porous assemblages consistently display strong coupling when they are illuminated with lights of different wavelengths, i.e., 400, 600, 800, and 1000 nm, albeit with varying field enhancement profiles.

We have further investigated the photothermal effect of the nanostructures in the solid state. As demonstrated in Figure S3, the nanostructures were deposited on the surface of a filter paper through a vacuum filtration process. The digital images of the films show a color similar to the dispersion, respectively (Figure 4d). The strong photothermal effect can also be visually recorded by an infrared thermal camera, as shown in Figure 4d. The white area indicates that the temperature is over 105 °C. As expected, S-35 shows the best photothermal performance in the solid state. Figure 4e exhibits the real-time temperature changes of the films during the illumination of the xenon light for 5 min. For all of the samples, the temperature increased in the first 3 min and then reached the plateau. The filter paper itself showed only a temperature increase of 20 °C, while those loaded with AgNP assemblages could attain much higher temperatures. As one would expect, the filter paper loaded with S-35 showed the highest heating rates, suggesting the most efficient photothermal conversion.

Over the past decades, significant efforts have been made to generate or collect clean water. Conventional solar steam generation requires materials high in optical density and typically suffers from high heat loss because the accumulated heat is transferred to the bulk water. To overcome this issue, we propose to heat only the surface water by localized surface heating of a layer of light-absorbing materials floating at the air—water interface, <sup>25–29</sup> illustrated in Figure 5a. In this case, the as-prepared Ag nanostructures were deposited on a filter paper by vacuum filtration. As shown in Figure S4, the filter paper was highly porous, which could facilitate the water transfer through the capillary interactions. The nanostructure films with controlled thickness were tightly attached to the surface of the filter paper (Figure S4). Furthermore, the filter paper also played a role in heat insulation, which could hinder the heat transfer from Ag to bulk water. Upon light illumination, the Ag nanostructures can effectively harvest light and convert its energy to heat through the photothermal effect. The accumulated heat would directly heat the surface water and produce vapor. At the same time, the superficial water was pumped to the heating layer by capillary force generated by the interaction of water and the porous filter paper. The generated steam would be condensed and collected to obtain clean water. The infrared thermal imaging technique was employed to monitor the localized heating behavior. As shown in the first row of Figure 5b, a beaker of water was placed below the xenon light as a control group, while the film loaded with S-35 was placed on the surface of the water in the experiment group (the second row). When the light was off, the two beakers showed the same temperature of ~20 °C. After light illumination for 5 min, the color of the air-water interface in the S-35 group changed to yellow-red in the IR thermal image, indicating that the surface water had been heated. However, the temperature of water in the control group had only negligible variation. After 15 min of illumination, the S-35 group showed a much higher temperature in the upper half ( $\sim$ 56 °C) than the lower half ( $\sim$ 36 °C) of the water, while in the control group the entire volume of water was heated to a medium temperature (~45 °C). These results clearly indicate that the black film at the water-air interface can efficiently harvest solar energy and promote local heating, which is beneficial to steam generation.

The steam generation performance of the black Ag films has been further quantified by plotting the mass change due to water evaporation as a function of the illumination time under the irradiation of a xenon lamp (Figure S5) and solar simulator (Figure 5c). The Ag assemblages show similar steam generation performance in both cases, which means the xenon lamp can be used to study the photothermal conversion performance of Ag assemblages (Figure 4d,e and Figure 5e). To more rigorously evaluate the steam generation rate and efficiency of Ag assemblages, we used the solar simulator in the later experiments. We first excluded the influence of filter paper to the water loss. Upon light illumination, water with its top surface covered by a filter paper showed a slightly smaller amount of water loss, indicating that the filter paper mainly reflects rather than absorbs light. When the AgNP assemblages were loaded on top of the filter paper, a significant enhancement in water loss can be observed. Upon light illumination for 1 h, the weight loss of the S-35 sample showed the steepest slope, indicating the best performance in steam generation. Figure 5d summarizes the relationship between samples with varied amounts of precursor and the evaporation rate. When the amount of Ag-ACN precursor increased from 15 to 25  $\mu$ L (S-15 and S-25), the coupling effect in Ag nanostructures became stronger, resulting in the enhanced performance in steam generation. The samples with black color (S-25, S-35, and S-45) displayed a more significant plasmonic coupling effect and accordingly exhibited better performance in steam generation. However, adding too much precursor to the reaction system (S-55 and S-65) led to interparticle fusion, therefore reducing the random coupling effect, caused a large shift of the plasmonic resonance to near-infrared region, and significantly increased the contribution of scattering in the extinction profile. As a result, the evaporation rate decreased.

In order to further evaluate the thermal performance of Ag assemblages, we utilize eq 1 to calculate the evaporation efficiency  $(\eta)$ , which is also known as the light-to-heat conversion efficiency.

$$\eta = \frac{\dot{m}h_{\rm LV}}{I} \tag{1}$$

where  $\dot{m}$  is the mass flux,  $h_{\rm LV}$  is the total enthalpy of liquid vapor phase change, and *I* is the power density of solar energy. The calculated solar steam generation efficiencies are shown in Figure 5D (green curve). The steam generation efficiency of Ag assemblages (S-35) can reach as high as 95.2%, while the substrate (filter paper) only shows an efficiency of 7.3%. The photothermal conversion efficiency of our system is among the highest on the basis of the comparison of our value to that of many references (Supporting Information, Table S1). We ascribe the high efficiency of the black Ag film to two key features: (i) the broadband absorption of Ag assemblages due to the strong random plasmonic coupling; (ii) the restricted thermal diffusion due to the low thermal conductivity of the paper substrate. First, most importantly, the black Ag film (S-35) shows a 13-fold higher efficiency toward steam generation than blank paper (control group), indicating that Ag nanostructures can harvest more solar energy and then efficiently convert it to heat. At the same time, the degree of plasmonic coupling, tuned by the amount of precursor, also greatly affects the steam generation efficiency. The samples with black color (S-25, S-35, and S-45) displayed a more significant plasmonic coupling effect and accordingly exhibited improved efficiency of 63.5%, 95.2%, and 87.3% in steam generation, respectively. Second, filter paper impedes thermal diffusion to the nonevaporative portion of the liquid by suppressing the conduction process. The microstructures of

the filter paper can also help suppress local convection. Both the reduced thermal conductivity and the suppressed convection contribute to the reduced heat loss from the evaporative surface to the bulk water.

The stability of the AgNP assemblages in the S-35 sample was studied through cycling experiments. As shown in Figure 6a, the water evaporation rate remained at the same level after

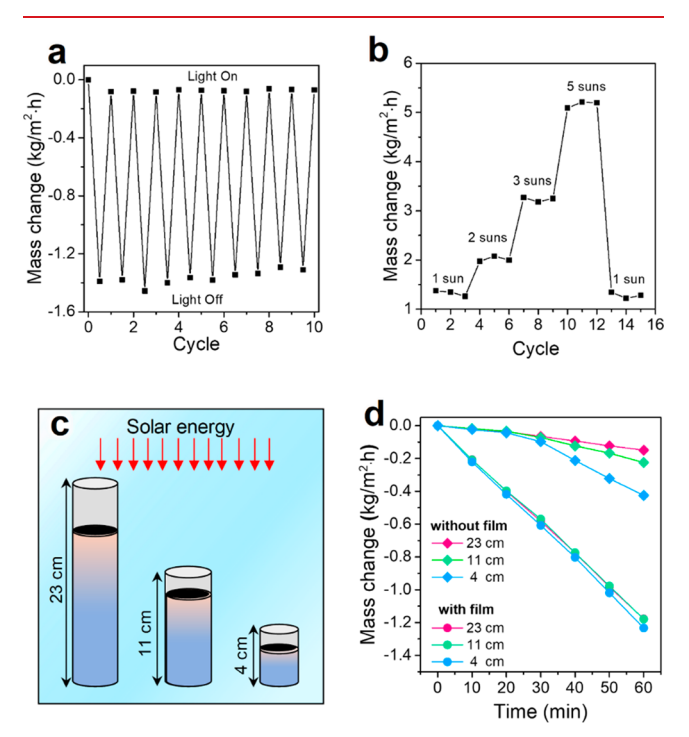


Figure 6. (a) Evaporation cycle performance of black Ag nanomaterials under 1 sun. (b) Evaporation cycle performance of an S35 film under different solar concentrations. (c) Schematics showing the setup for studying the dependence of evaporation efficiency on water quantity using beakers of the same diameter (4 cm) but different water heights. (d) Mass change over time for water samples of different heights with and without the coverage of black Ag films on the top surface.

1 h of illumination and cooling for 10 cycles, indicating good thermal stability of the Ag nanostructures. After 10 cycles of light irradiation, the AgNP assemblages were found to be able to maintain their original structure (Figure S6), further confirming their high stability. In addition, the stability of Ag nanostructures has been tested under light illumination with different powers. As shown in Figure 6b, when the power of the incident light increased from 1 to 5 suns, the evaporation rate of water increased from 1.38 to 5.21 kg/(m²·h). When the power returned to 1 sun, the black film showed an evaporation rate of  $\sim\!1.32$  kg/(m²·h), which was the same as the original value, further confirming the excellent stability of the Ag nanostructures under harsh illumination conditions.

To further demonstrate the localized heating effect, we studied the dependence of efficiencies on water quantities. The experimental setup is illustrated in Figure 6c. Glass tubes with the same diameters but different heights (23, 11, and 4 cm) were chosen as the water containers. Black films composed of the same amount of Ag nanostructures were used as light absorbing materials for steam generation, and the mass change of water in each container was plotted against the illumination time. For comparison, the water losses of the samples without

the black films were also studied. As shown in Figure 6d, without Ag films, the water losses of the three samples were the same during the first 20 min of light illumination and varied considerably with water quantities thereafter. In this case, light was used to heat the entire volume of water, so the evaporation rate remained the same until the water temperature (which depended on the volume of water) became significantly different at the later stage. In contrast, when black Ag films were placed on top of the water, the water loss profile did not show apparent dependence on the water volume (Figure 6d), because the light was absorbed primarily by the black film and the resulting heat was used to drive water evaporation near the water/air interface.

To demonstrate its performance for steam generation in a real setting, we illuminated a black Ag film floating on the surface of water by the natural sunlight (Figure S7a). When the black Ag film was irradiated with sunlight, the steam was generated and condensed to the right side of the homemade container. We recorded the changes in water mass and solar power of the sunlight at different times within 1 day (Figures S7b and S7c). The solar intensity increased from 0.689 kW/m<sup>2</sup> at 10 a.m. to 0.943 kW/m<sup>2</sup> at 2 p.m., and the mass change rate changed from 0.34 to 0.93 kg/(m<sup>2</sup>·h) accordingly. In the afternoon, the solar intensity came down, so that the mass change rate consistently decreased to 0.65 kg/(m<sup>2</sup>·h) at 4 p.m. The light-to-heat conversion efficiencies at different times were also calculated through eq 1. As shown in Figure S7c, the variation trend of steam generation efficiency is consistent with the changes in the solar intensity. Our materials attain the highest steam generation efficiency of 68.3% at 2 p.m. with the irradiation of natural sunlight.

In summary, we report a unique confined seeded growth strategy for the synthesis of black silver nanostructures with broadband absorption in the visible and near-IR spectrum for efficient solar steam generation. The controlled seeded growth confined within a nanoscale tubular space enables the formation of rod-shaped assemblages of AgNPs with well-distributed interparticle distances. The resulting strong random plasmonic coupling leads to broadband absorption in the visible and near-IR spectrum, producing black Ag nanostructures with excellent efficiency in converting solar energy to heat. The AgNP assemblages can be fabricated in the form of thin films floating at the air/water interface, which show exceptional performance in generating clean water steam through localized interfacial heating.

## ASSOCIATED CONTENT

# **S** Supporting Information

The Supporting Information is available free of charge on the ACS Publications website at DOI: 10.1021/acs.nanolett.8b04157.

Details of the experiments, near electromagnetic field of AgNP chains, absorption spectra, schematic illustration of the preparation of Ag assemblages film, SEM image of Ag assemblages loaded on filter paper, time course of water evaporation performance under 1 sun by a xenon lamp, TEM image of AgNPs assemblanges after irradiation, steam generation under natural sun, and summary of steam generation efficiency data in the literature (PDF)

#### AUTHOR INFORMATION

#### **Corresponding Authors**

\*Mozhen Wang. Tel: +86 138-6614-3146. E-mail: pstwmz@ustc.edu.cn.

\*Yadong Yin. Tel: 951-827-4965. E-mail: yadong.yin@ucr.edu.

#### ORCID ®

Mozhen Wang: 0000-0003-2408-1805 Yadong Yin: 0000-0003-0218-3042

#### **Author Contributions**

The manuscript was written through contributions of all authors.

# Notes

The authors declare no competing financial interest.

## ACKNOWLEDGMENTS

Y.Y. acknowledges the support from the U.S. National Science Foundation (CHE-1808788). J.C. thanks the fellowship support by the China Scholarship Council (CSC). Acknowledgment is also made to the Donors of the American Chemical Society Petroleum Research Fund for partial support of this research. M.W. acknowledges the support from the National Natural Science Foundation of China (No. 51573174). The authors also thank the Central Facility for Advanced Microscopy and Microanalysis at UCR for help with TEM analysis.

## REFERENCES

- (1) Elimelech, M.; Phillip, W. A. Science 2011, 333, 712-717.
- (2) Hogan, N. J.; Urban, A. S.; Ayala-Orozco, C.; Pimpinelli, A.; Nordlander, P.; Halas, N. *Nano Lett.* **2014**, *14*, 4640–4645.
- (3) Liu, G.; Xu, J.; Wang, K. Nano Energy 2017, 41, 269-284.
- (4) Zhang, L.; Tang, B.; Wu, J.; Li, R.; Wang, P. Adv. Mater. 2015, 27, 4889-4894.
- (5) Zhou, L.; Tan, Y.; Wang, J.; Xu, W.; Yuan, Y.; Cai, W.; Zhu, S.; Zhu, J. Nat. Photonics **2016**, 10, 393-398.
- (6) Zielinski, M. S.; Choi, J. W.; La Grange, T.; Modestino, M.; Hashemi, S. M.; Pu, Y.; Birkhold, S.; Hubbell, J. A.; Psaltis, D. *Nano Lett.* **2016**, *16*, 2159–2167.
- (7) Clavero, C. Nat. Photonics 2014, 8, 95-103.
- (8) Kristensen, A.; Yang, J. K. W.; Bozhevolnyi, S. I.; Link, S.; Nordlander, P.; Halas, N. J.; Mortensen, N. A. *Nat. Rev. Mater.* **2017**, 2, 16088–16102.
- (9) Bae, K.; Kang, G.; Cho, S. K.; Park, W.; Kim, K.; Padilla, W. J. Nat. Commun. **2015**, 6, 10103–10112.
- (10) Piella, J.; Bastús, N. G.; Puntes, V. Chem. Mater. 2016, 28, 1066-1075.
- (11) Huang, J.; Liu, C.; Zhu, Y.; Masala, S.; Alarousu, E.; Han, Y.; Fratalocchi, A. *Nat. Nanotechnol.* **2016**, *11*, 60–66.
- (12) Jiang, K.; Smith, D. A.; Pinchuk, A. J. Phys. Chem. C 2013, 117, 27073–27080.
- (13) Chen, H.; Shao, L.; Ming, T.; Sun, Z.; Zhao, C.; Yang, B.; Wang, J. Small **2010**, *6*, 2272–2280.
- (14) Liu, D.; Zhou, F.; Li, C.; Zhang, T.; Zhang, H.; Cai, W.; Li, Y. Angew. Chem., Int. Ed. **2015**, 54, 9596–9600.
- (15) Randrianalisoa, J.; Li, X.; Serre, M.; Qin, Z. Adv. Opt. Mater. **2017**, 5, 1700403–1700414.
- (16) Halas, N. J.; Lal, S.; Chang, W. S.; Link, S.; Nordlander, P. Chem. Rev. 2011, 111, 3913–3961.
- (17) Anker, J. N.; Hall, W. P.; Lyandres, O.; Shah, N. C.; Zhao, J.; Van Duyne, R. P. *Nat. Mater.* **2008**, *7*, 442–453.
- (18) Steiner, A. M.; Mayer, M.; Seuss, M.; Nikolov, S.; Harris, K. D.; Alexeev, A.; Kuttner, C.; Konig, T. A. F.; Fery, A. ACS Nano 2017, 11, 8871–8880.
- (19) Xia, Y.; Gilroy, K. D.; Peng, H. C.; Xia, X. Angew. Chem., Int. Ed. **2017**, 56, 60–95.

(20) Zhu, C.; Zeng, J.; Tao, J.; Johnson, M. C.; Schmidt-Krey, I.; Blubaugh, L.; Zhu, Y.; Gu, Z.; Xia, Y. J. Am. Chem. Soc. **2012**, 134, 15822–15831.

- (21) Liu, X.; Li, L.; Yang, Y.; Yin, Y.; Gao, C. Nanoscale 2014, 6, 4513-4516.
- (22) Liu, X.; Yin, Y.; Gao, C. Langmuir 2013, 29, 10559-10565.
- (23) Cai, J.; Qi, L. Mater. Horiz. 2015, 2, 37-53.
- (24) Zhou, L.; Tan, Y.; Ji, D.; Zhu, B.; Zhang, P.; Xu, J.; Gan, Q.; Yu, Z.; Zhu, J. Sci. Adv. 2016, 2, e1501227.
- (25) Li, X.; Xu, W.; Tang, M.; Zhou, L.; Zhu, B.; Zhu, S.; Zhu, J. Proc. Natl. Acad. Sci. U. S. A. 2016, 113, 13953-13958.
- (26) Xu, N.; Hu, X.; Xu, W.; Li, X.; Zhou, L.; Zhu, S.; Zhu, J. Adv. Mater. **2017**, 29, 1606762–1606767.
- (27) Zhou, L.; Tan, Y.; Ji, D.; Zhu, B.; Zhang, P.; Xu, J.; Gan, Q.; Yu, Z.; Zhu, J. Sci. Adv. 2016, 2, e1501227.
- (28) Shi, Y.; Li, R.; Jin, Y.; Zhuo, S.; Shi, L.; Chang, J.; Hong, S.; Ng, K.-C.; Wang, P. Joule **2018**, 2, 1171.
- (29) Li, X.; Li, J.; Lu, J.; Xu, N.; Chen, C.; Min, X.; Zhu, B.; Li, H.; Zhu, L.; Zhu, S.; Zhang, T.; Zhu, J. *Joule* **2018**, *2*, 1331.